Adaptivity, sensitivities and uncertainties in CFD

A. Hay[1], S. Etienne[2] and D. Pelletier[2]

[1] Interdisciplinary Center for Applied Mathematics, Virginia Tech, Blacksburg, VA 24061, USA

[2] Département de Génie Mécanique, Ecole Polytechnique de Montréal, Montréal (Québec), CANADA, H3C 3A7

Abstract

We present Verification & Validation (V&V) results for an adaptive finite element turbulent flow and sensitivity solver. The three essential steps in V&V - Code Verification, Solution Verification, and Validation - are carried out as recommended by standards of good practice in CFD. Verification of the solvers, adaptive procedure and single grid error estimators (for global, surface integral or pointwise quantities) are performed all at once for wall bounded turbulent flows using the Method of the Manufactured Solution. Solution Verification is then carried out on the ERCOFTAC test case C-30, a backward facing step and on the turbulent flow over a square obstacle in proximity of a flat plate. Grid independent results with error estimations are achieved using the verified adaptive methodology and single-grid error evaluation procedures. Finally, Validation of numerical results for the square cylinder flows is carried out by examining comparisons to experimental data. In addition, the paper explores the Sensitivity Equation Method (SEM) as a tool to perform uncertainty analysis of CFD predictions in the context of Validation. Sensitivity Analysis can yield estimates of uncertainty of the flow response to uncertainties or inaccuraccies in the data input to the flow solver.

1 Introduction

Accurate and reliable predictions of fluid flows have been the topic of much research by the CFD community over the past several years. A review of the literature reveals that, in many cases, predictions of a given flow by different authors show unexpectedly large scatter. This can be especially disconcerting when people produce vastly different predictions while using similar models and numerical methods. Thus, the question of the error associated to numerical solutions arises to determine to which extent a solution is reliable. Irrespective of the quality of a mathematical model, the accuracy of a numerical procedure or the attention paid to numerical linear solver, an error will always exist. The quantification of this error is of great importance since it ascertains the trust that one can legitimately have in the computed solution. Experimental data are always reported with uncertainty bars. Surprisingly, it is not a common practice for numerical results. However, a growing effort has been undertaken by the computational science community to quantify uncertainty in computer simulations. In Computational Fluid Dynamics (CFD) this endeavour has led to a broad discussion on Verification and Validation (V&V) by several organizations such as the AIAA, the ASME, the ERCOFTAC or the ITTC Resistance Committee. Two workshops on CFD Uncertainty Analysis have been held in Lisbon [1, 2] bringing together people concerned about the reliability of their computational results. Such discussions have succeeded establishing standardized procedures. However, open questions still remain and some more progress needs to be achieved in the V&V discipline.

The different types of errors associated to a numerical solution can be classified with the taxonomy proposed by Oberkampf *et al.* [3] or Ferziger and Perić [4]. Such a taxonomy is meaningful and adequate in the context of V&V as demonstrated by Roache in Ref. [5]. Each type of error associated to a numerical solution falls in one of the following five categories :

Hay, A.; Etienne, S.; Pelletier, D. (2007) Adaptivity, Sensitivities and Uncertainties in CFD. In *Computational Uncertainty in Military Vehicle Design* (pp. 8-1 – 8-28). Meeting Proceedings RTO-MP-AVT-147, Paper 8. Neuilly-sur-Seine, France: RTO. Available from: http://www.rto.nato.int.

1. modeling error
2. discretization error
3. iteration error
4. programming error
5. computer round-off error

For the present study, we assumed that codes use a sufficiently robust linear solver to reduce the algebraic residuals of the discretized equations to machine precision ensuring that the iteration errors on the computed solutions are negligible. Furthermore, double precision computations are performed so that the computer round-off error are not significant compared to the other sources of error. We are left thus with programming errors, discretization errors and physical modeling errors. These three types of errors can be directly related to the three essential steps in Verification and Validation as discussed in Roache's book [5] :

1. Code Verification
2. Solution Verification
3. Validation

Verification is defined as a synonym for solving the equations accurately (*Solving the equations right*). Hence, Verification is essentially and strictly in mathematical and numerical analysis and performed in two steps The first one is *Code Verification* which aims at identifying and removing any programming error. Once this step is completed, one can focus on the other types of errors having full confidence in the solver at hand. Furthermore, the effective convergence rate of the numerical methods used is assessed numerically during this first step. The Method of the Manufactured Solution (MMS) [6] provides a rigorous framework to easily perform Code Verification. Moreover, the performance of the error estimation procedures used during the second verification step can also be assessed by comparison to true errors. In V&V, the most popular practice to analyse grid convergence and to provide uncertainty measures of numerical predictions is the use of the Grid Convergence Index (GCI) [7, 5]. It computes reliable error bars by applying safety factors on error estimates obtained from Richardson extrapolation. Its successes, difficulties and failures have already been reported for example in Refs. [7, 8, 9]. However, it requires to compute solutions on at least three grids and often more [9]. Thus, the GCI can not report errors from a single grid computation. Here, we propose the use of single-grid recovery-based error estimators to produce error estimates for global norms and for pointwise quantities. These estimates are compared to the true errors to assess their reliability. That is, we perform *the verification of the verification procedure*. Code Verification is performed for an Adaptive Finite Element Solver driven by error estimates for turbulent flows and sensitivities.

The second step, *Solution Verification*, aims at evaluating the discrepancy between the exact solution to the differential equations modeling the phenomenom of interest and the exact solution to the algebraic equations arising from discretization. As mentioned earlier, we assume that computer round-off and iteration errors are negligible. In this case, Solution Verification reduces to the evaluation of discretization errors caused by, among other things :

- the choice of polynomial interpolation function for finite element approximations, or of flux evaluation in finite volume methods,
- the distribution of computational cell sizes,
- the representation and interpolation of boundary conditions,
- the discretization of curved geometries,
- discretization of data such as temperature dependent fluid properties or the eddy viscosity,
- nonlinear mixed boundary conditions.

All these aspects are within the control of the analyst. Grid refinement studies can be performed and error estimates can be obtained. Adaptive methods are an especially good tool for assessing and controling these errors, that is verifying a given simulation. We illustrate this for incompressible turbulent flows over a backward facing step where grid independent predictions are certified using mesh adaptivity. Error estimates on global, local and integral quantities provide several measures of the reliability of the numerical results.

The third step, *Validation*, is the process of determining if the right equations are solved for the process at hand (*Solving the right equations*). It is essentially and strictly an engineering activity involving comparition with laboratory or field data. It goes without saying that one performs Validation only with *verified simulations* obtained with *verified code*. This is illustrated here for the turbulent flow over a square obstacle in proximity of a flat plate where numerical results from our adaptive finite-element solver are compared to the Laser Doppler Velocimetry measurements of Wu and Martinuzzi [10]. However, to make this exercise truly meaningful, one must account for uncertainties in both measurements and in the input parameters to the flow solver. Input parameters to a CFD code fall in two categories : value and shape parameters. A value parameter does not affect the shape of the computational domain. Typical examples include : values of physical properties (say viscosity), a closure coefficient in a turbulence model, a boundary condition, a constant in a constitutive equations, etc. A shape parameter affects the geometry of the computational domain. Examples include the details of geometry of an airfoil, its angle of attack, the relative position of a slat or flap, etc. All such input parameters are prescribed to a certain level of accuracy or uncertainty which has a direct impact on the accuracy/uncertainty of the CFD solution. For example, a least-squares correlation of viscosity as a function of temperature may be accurate to say 6% [11], while an angle of attack my be measured to within say .1 degrees. Finally, manufacturing tolerances result in uncertainties in the geometrical data. All these uncertainties are beyond the control of the analysts. Yet they must be accounted for to achieve meaningful comparisons with measurements. In this paper, we show how sensitivity information can be used to provide uncertainty intervals for the CFD solution computed at the nominal values of the parameters. The resulting uncertainty bars put CFD *on par* with experimental techniques and provide a tool to assess to what extent these *accurate* solution can be trusted. The larger the uncertainty of the flow response the lower the confidence.

The paper is organized as follows. Section 2 presents the modeling equations for turbulent flows and their sensitivities. In Section 3, the finite element formulation and adaptive remeshing is described along with the error estimation procedure. Code Verification by the Method of the Manufactured Solution is presented in Section 4. Moreover, the performance of the error estimator is evaluated. Section 5 considers the flow over a backward facing-step to perform Solution Verification with mesh adaptation. Validation and Uncertainty analysis of CFD results is reported in Section 6 for the flow of air around a square cross-section cylinder in the proximity of a solid wall.

2 Turbulent Flows and Sensitivity Analysis

2.1 Turbulent Flow Modeling

The flows of interest are described by the Reynolds-Averaged Navier-Stokes (RANS) equations. The momentum and mass conservation laws are written as :

$$\rho \mathbf{u} \cdot \nabla \mathbf{u} = -\nabla p + \nabla \cdot \tau(\mathbf{u}) + \mathbf{f} \quad (1)$$

$$\nabla \cdot \mathbf{u} = 0 \quad (2)$$

where ρ is the density, $\mathbf{u}$ the velocity, p the pressure and $\mathbf{f}$ the volumetric forces. Noting μ the molecular dynamic viscosity and μ_t the turbulent dynamic viscosity, the stress tensor τ is defined according to the newton's law and the first order turbulence modelization approximation :

$$\tau(\mathbf{u}) = (\mu + \mu_t) \left[\nabla \mathbf{u} + (\nabla \mathbf{u})^T \right]$$

The system is closed by computing the turbulent viscosity using the $k-\epsilon$ model. The eddy viscosity is computed from k and ϵ by :

$$\mu_t = \rho C_\mu \frac{k^2}{\epsilon} \tag{3}$$

To preserve positivity of the dependent variables, we work with the logarithmic form of these equations [12]. This can be viewed as using the following change of dependent variables :

$$\mathcal{K} = \ln(k) \qquad \text{and} \qquad \mathcal{E} = \ln(\epsilon) \tag{4}$$

The transport equations for the logarithmic variables are :

$$\begin{aligned} \rho \mathbf{u} \cdot \nabla \mathcal{K} = \nabla \cdot \left[\left(\mu + \frac{\mu_t}{\sigma_k} \right) \nabla \mathcal{K} \right] + \left(\mu + \frac{\mu_t}{\sigma_k} \right) \nabla \mathcal{K} \cdot \nabla \mathcal{K} \\ + \mu_t e^{-\mathcal{K}} P - \rho^2 C_\mu \frac{e^{\mathcal{K}}}{\mu_t} + q_{\mathcal{K}} \end{aligned} \tag{5}$$

$$\begin{aligned} \rho \mathbf{u} \cdot \nabla \mathcal{E} = \nabla \cdot \left[\left(\mu + \frac{\mu_t}{\sigma_\epsilon} \right) \nabla \mathcal{E} \right] + \left(\mu + \frac{\mu_t}{\sigma_\epsilon} \right) \nabla \mathcal{E} \cdot \nabla \mathcal{E} \\ + \rho C_1 C_\mu e^{\mathcal{K}-\mathcal{E}} P - C_2 \rho e^{\mathcal{E}-\mathcal{K}} + q_{\mathcal{E}} \end{aligned} \tag{6}$$

The production of turbulence P is defined as :

$$P = \nabla \mathbf{u} : \left[\nabla \mathbf{u} + (\nabla \mathbf{u})^T \right]$$

The constants appearing in these equations take on the standard values proposed by Launder and Spalding [13] and are given in Table 1. Note that equations (5)-(6) are equivalent to the original equations of the

Table 1: Constant of the turbulence model

σ_k	σ_ϵ	$C_{\epsilon 1}$	$C_{\epsilon 2}$	C_μ
1.0	1.3	1.44	1.92	0.09

turbulence model; only the computational variables are different. Hence, the turbulence model is unchanged. The eddy viscosity is given by :

$$\mu_t = \rho C_\mu e^{2\mathcal{K}-\mathcal{E}} \tag{7}$$

2.1.1 Classical Dirichlet and Neumann boundary conditions

Boundaries of Ω that are not walls are modeled using standard Dirichlet and Neumann boundary conditions. They are imposed on boundaries Γ_D and Γ_N respectively :

- Dirichlet boundary conditions :

$$\mathbf{u} = \overline{\mathbf{u}} \quad ; \quad \mathcal{K} = \ln(\beta_k) \quad ; \quad \mathcal{E} = \ln(\beta_\epsilon) \tag{8}$$

- Neumann boundary conditions :

$$[-p\mathbf{I} + \tau(\mathbf{u})] \cdot \hat{\mathbf{n}} = \overline{\mathbf{t}} \quad ; \quad \left[\left(\mu + \frac{\mu_t}{\sigma_k} \right) \nabla \mathcal{K} \right] \cdot \hat{\mathbf{n}} = 0 \quad ; \quad \left[\left(\mu + \frac{\mu_t}{\sigma_\epsilon} \right) \nabla \mathcal{E} \right] \cdot \hat{\mathbf{n}} = 0 \tag{9}$$

where $\hat{\mathbf{n}}$ is an outward unit vector normal to the boundary, $\mathbf{I}$ the second order identity tensor and β_k and β_ϵ small constants.

2.1.2 Wall boundary conditions

The standard $k-\epsilon$ turbulence model is not valid when the turbulent Reynolds number is low, as it is the case in near wall regions. Wall functions are used to describe the solution in these areas. The computational boundary is set at a distance d from the physical wall boundary. The gap between these two boundaries is the region where the flow is represented by the wall functions instead of being solved. In the remainder, the computational wall boundary will be referred to as the wall and quantities evaluated at it will be identified with the subscript w. We utilize the two-velocity scale wall functions described by Chabard [14] and Ignat *et al* [15] and presented in what follows.

A wall function expresses the value of u^+, the non-dimensional velocity parallel to the solid wall, as a function of y^+, the non-dimensional distance from the physical wall :

$$u^+ = \frac{1}{\kappa}\ln(Ey^+) \qquad \text{for} \qquad y^+ > 10.8 \tag{10}$$

where κ is the Karman constant and E a roughness parameter (for smooth walls we take $\kappa = 0.42$ and $E = 9.0$). The variables u^+ and y^+ are defined as follows :

$$y^+ = \frac{\rho d u_k}{\mu} \qquad \text{and} \qquad u^+ = \frac{u_t}{u_{**}} \tag{11}$$

where $u_t = \mathbf{u}\cdot\hat{\mathbf{t}}$ denotes the tangential velocity, d is the normal distance to the physical wall and $u_{**} = \sqrt{\tau_w/\rho}$ the friction velocity. The specific value of d where the wall function is applied is chosen so that y^+ lies within the range of validity of the function (i.e. $30 < y^+ < 300$) [16]. A velocity scale based on the turbulence kinetic energy [14] is computed by :

$$u_k = C_\mu^{\frac{1}{4}} k_w^{\frac{1}{2}} = C_\mu^{\frac{1}{4}} \exp\left(\frac{\mathcal{K}_w}{2}\right) \tag{12}$$

The boundary conditions associated to the governing equations are :

- flow boundary condition in the tangential direction : the constraint applied by the flow to the wall in the tangential direction is prescribed as a function of the tangential velocity (mixed or Robin boundary condition). Using the two-velocity scale wall function leads to a linear relationship between the shear stress at the wall τ_w in the direction of the flow and u_t.

$$\left[(\tau\cdot\hat{\mathbf{n}})\cdot\hat{\mathbf{t}}\right]_{wall} = \tau_w = \rho u_k u_{**} = \frac{\rho u_k}{\frac{1}{\kappa}\ln(E\frac{\rho d u_k}{\mu})} u_t \tag{13}$$

- flow boundary condition in the normal direction : the normal velocity is set to zero.

$$\mathbf{u}\cdot\hat{\mathbf{n}} = 0 \tag{14}$$

- boundary condition for $\mathcal{K}$: The $\mathcal{K}$-equation is solved with a zero auxiliary flux boundary condition. This condition arises from the fact that the wall shear stress is considered constant in the wall functions region (i.e. $0 < y^+ < 300$) [16]. This Neumann condition is required to compute the distribution of u_k along the wall.

$$\left(\mu + \frac{\mu_t}{\sigma_k}\right)\nabla\mathcal{K}\cdot\hat{\mathbf{n}} = 0 \tag{15}$$

- boundary condition for $\mathcal{E}$: The boundary condition for the logarithm of ϵ is the logarithm of the usual Dirichlet boundary condition for the turbulence kinetic energy dissipation rate at walls but the velocity scaled u_k is used instead of u_{**}.

$$\mathcal{E} = \ln\left(\frac{u_k^3}{\kappa d}\right) \tag{16}$$

2.2 Continuous Sensitivity Equations

The Continuous Sensitivity Equations are derived formally by direct differentiation of the flow equations (Eqs. (1)-(2)) and the turbulence variables equations (Eqs. (5)-(6)) with respect to an arbitrary parameter a. Thus, we treat any variable $\mathbf{u}$ as a function of both space and parameter a. This dependency is denoted by $\mathbf{u} = \mathbf{u}(\mathbf{x}; a)$. The sensitivities are defined as the partial derivatives :

$$\mathbf{s_u} = \frac{\partial \mathbf{u}}{\partial a} \quad ; \quad s_p = \frac{\partial p}{\partial a} \quad ; \quad s_{\mathcal{K}} = \frac{\partial \mathcal{K}}{\partial a} \quad ; \quad s_{\mathcal{E}} = \frac{\partial \mathcal{E}}{\partial a} \tag{17}$$

Then, CSE governing sensitivity fields are written as :

$$\rho' \mathbf{u} \cdot \nabla \mathbf{u} + \rho \left(\mathbf{s_u} \cdot \nabla \mathbf{u} + \mathbf{u} \cdot \nabla \mathbf{s_u} \right) = -\nabla s_p + \nabla \cdot \tau(\mathbf{s_u}) + \nabla \cdot \tau'(\mathbf{u}) + \mathbf{f}_s \tag{18}$$

$$\nabla \cdot \mathbf{s_u} = 0 \tag{19}$$

$$\begin{aligned} \rho' \mathbf{u} \cdot \nabla \mathcal{K} + \rho \left(\mathbf{s_u} \cdot \nabla \mathcal{K} + \mathbf{u} \cdot \nabla s_{\mathcal{K}} \right) &= \nabla \cdot \left[\left(\mu' + \frac{\mu_t'}{\sigma_k} - \frac{\mu_t \sigma_k'}{\sigma_k^2} \right) \nabla \mathcal{K} + \left(\mu + \frac{\mu_t}{\sigma_k} \right) \nabla s_{\mathcal{K}} \right] \\ &+ \left(\mu' + \frac{\mu_t'}{\sigma_k} - \frac{\mu_t \sigma_k'}{\sigma_k^2} \right) \nabla \mathcal{K} \cdot \nabla \mathcal{K} \\ &+ 2 \left(\mu + \frac{\mu_t}{\sigma_k} \right) \nabla \mathcal{K} \cdot \nabla S_{\mathcal{K}} + e^{-\mathcal{K}} \left(\mu_t' P + \mu_t P' - \mu_t P s_{\mathcal{K}} \right) \\ &- \rho e^{\mathcal{E} - \mathcal{K}} \left(2 \frac{\rho'}{\rho} + \frac{C_\mu'}{C_\mu} + s_{\mathcal{K}} - \frac{\mu_t'}{\mu_t} \right) \end{aligned} \tag{20}$$

$$\begin{aligned} \rho' \mathbf{u} \cdot \nabla \mathcal{E} + \rho \left(\mathbf{s_u} \cdot \nabla \mathcal{E} + \mathbf{u} \cdot \nabla s_{\mathcal{E}} \right) &= \nabla \cdot \left[\left(\mu' + \frac{\mu_t'}{\sigma_\epsilon} - \frac{\mu_t \sigma_\epsilon'}{\sigma_\epsilon^2} \right) \nabla \mathcal{E} + \left(\mu + \frac{\mu_t}{\sigma_\epsilon} \right) \nabla s_{\mathcal{E}} \right] \\ &+ \left(\mu' + \frac{\mu_t'}{\sigma_\epsilon} - \frac{\mu_t \sigma_\epsilon'}{\sigma_\epsilon^2} \right) \nabla \mathcal{E} \cdot \nabla \mathcal{E} + 2 \left(\mu + \frac{\mu_t}{\sigma_\epsilon} \right) \nabla \mathcal{E} \cdot \nabla S_{\mathcal{E}} \\ &+ \rho C_{\epsilon 1} C_\mu e^{\mathcal{K} - \mathcal{E}} P \left(\frac{\rho'}{\rho} + \frac{C_{\epsilon 1}'}{C_{\epsilon 1}} + \frac{C_\mu'}{C_\mu} + S_{\mathcal{K}} - S_{\mathcal{E}} + \frac{P'}{P} \right) \\ &- C_{\epsilon 2} \rho e^{\mathcal{E} - \mathcal{K}} \left(\frac{C_{\epsilon 2}'}{C_{\epsilon 2}} + \frac{\rho'}{\rho} + S_{\mathcal{E}} - S_{\mathcal{K}} \right) \end{aligned} \tag{21}$$

the partial derivatives of the fluid properties being denoted using a ($'$), $\mathbf{f}_s$ being the sensitivity of the volumetric forces and having :

$$\begin{aligned} \tau'(\mathbf{u}) &= (\mu' + \mu_t') \left[\nabla \mathbf{u} + (\nabla \mathbf{u})^T \right] \\ \tau(\mathbf{s_u}) &= (\mu + \mu_t) \left[\nabla \mathbf{s_u} + (\nabla \mathbf{s_u})^T \right] \\ P' &= 2 \nabla \mathbf{s_u} : \left[\nabla \mathbf{u} + (\nabla \mathbf{u})^T \right] \end{aligned}$$

with the sensitivity of the eddy-viscosity given by :

$$\mu_t' = \mu_t \left(\frac{\rho'}{\rho} + \frac{C_\mu'}{C_\mu} + 2 s_{\mathcal{K}} - s_{\mathcal{E}} \right) \tag{22}$$

Finally, the sensitivities of the turbulence variables and those of their logarithms are related through :

$$S_{\mathcal{K}} = \frac{S_k}{k} \quad ; \quad S_{\mathcal{E}} = \frac{S_\epsilon}{\epsilon} \tag{23}$$

2.2.1 Classical Dirichlet and Neumann boundary conditions

We first present the derivation of the classical Dirichlet and Neumann boundary conditions (Eqs. (8) and (9)). Only the material derivatives of these conditions are known. However, sensitivity boundary conditions are obtained by expressing the relationship between the material derivative and the sensitivity $\frac{\partial \phi}{\partial a}$. Doing so, the following boundary conditions are obtained.

- Dirichlet boundary condition on Γ_D :

$$\begin{aligned} \mathbf{s_u} &= \frac{D\overline{\mathbf{u}}}{Da} - \nabla \mathbf{u} \cdot \frac{\partial \hat{\mathbf{X}}}{\partial a} \\ s_{\mathcal{K}} &= \frac{\beta_k'}{\beta_k} - \nabla \mathcal{K} \cdot \frac{\partial \hat{\mathbf{X}}}{\partial a} \\ s_{\mathcal{E}} &= \frac{\beta_\epsilon'}{\beta_\epsilon} - \nabla \mathcal{E} \cdot \frac{\partial \hat{\mathbf{X}}}{\partial a} \end{aligned} \tag{24}$$

- Neumann boundary condition on Γ_N :

$$\begin{aligned} [-s_p \mathbf{I} + \tau'(\mathbf{u}) + \tau(\mathbf{s_u})] \cdot \hat{\mathbf{n}} &= \frac{D\overline{\mathbf{t}}}{Da} - \left[\nabla \left[-p\mathbf{I} + \tau(\mathbf{u}) \right] \cdot \frac{\partial \hat{\mathbf{X}}}{\partial a} \right] \cdot \hat{\mathbf{n}} \\ &\quad - \left[-p\mathbf{I} + \tau(\mathbf{u}) \right] \cdot \frac{\partial \hat{\mathbf{n}}}{\partial a} \end{aligned} \tag{25}$$

$$\begin{aligned} \left[\left(\mu' + \frac{\mu_t'}{\sigma_k} - \frac{\mu_t \sigma_k'}{\sigma_k^2} \right) \nabla \mathcal{K} + \left(\mu + \frac{\mu_t}{\sigma_k} \right) \nabla s_{\mathcal{K}} \right] \cdot \hat{\mathbf{n}} &= - \left[\nabla \mu \cdot \frac{\partial \hat{\mathbf{X}}}{\partial a} + \frac{\nabla \mu_t \cdot \frac{\partial \hat{\mathbf{X}}}{\partial a}}{\sigma_k} \right] \nabla \mathcal{K} \cdot \hat{\mathbf{n}} \\ &\quad - \left(\mu + \frac{\mu_t}{\sigma_k} \right) \left[\nabla \mathcal{K} \cdot \frac{\partial \hat{\mathbf{n}}}{\partial a} + \nabla \left(\nabla \mathcal{K} \right) \cdot \frac{\partial \hat{\mathbf{X}}}{\partial a} \cdot \hat{\mathbf{n}} \right] \end{aligned} \tag{26}$$

$$\begin{aligned} \left[\left(\mu' + \frac{\mu_t'}{\sigma_\epsilon} - \frac{\mu_t \sigma_\epsilon'}{\sigma_\epsilon^2} \right) \nabla \mathcal{E} + \left(\mu + \frac{\mu_t}{\sigma_\epsilon} \right) \nabla s_{\mathcal{E}} \right] \cdot \hat{\mathbf{n}} &= - \left[\nabla \mu \cdot \frac{\partial \hat{\mathbf{X}}}{\partial a} + \frac{\nabla \mu_t \cdot \frac{\partial \hat{\mathbf{X}}}{\partial a}}{\sigma_\epsilon} \right] \nabla \mathcal{E} \cdot \hat{\mathbf{n}} \\ &\quad - \left(\mu + \frac{\mu_t}{\sigma_\epsilon} \right) \left[\nabla \mathcal{E} \cdot \frac{\partial \hat{\mathbf{n}}}{\partial a} + \nabla \left(\nabla \mathcal{E} \right) \cdot \frac{\partial \hat{\mathbf{X}}}{\partial a} \cdot \hat{\mathbf{n}} \right] \end{aligned}$$

As can be seen, for a shape parameter, first derivatives of the flow and turbulence variables are needed to evaluate Dirichlet boundary conditions and second derivatives are required for evaluating Neumann boundary conditions. This introduces numerical difficulties when solving the CSE, since approximate boundary conditions are used. In practice, boundary conditions are evaluated using high order Taylor series expansions on layered patches in conjunction with a constrained least-square procedure [17].

2.2.2 Wall boundary conditions for sensitivities

The differentiation of the wall boundary conditions leads to the following boundary conditions for CSE.

- flow sensitivity boundary condition in the tangential direction :

$$\begin{aligned} \left[\left(\frac{\partial \tau}{\partial a} \cdot \hat{\mathbf{n}} \right) \cdot \hat{\mathbf{t}} \right]_{wall} &= \left(\rho' + \nabla \rho \cdot \frac{\partial \hat{\mathbf{X}}}{\partial a} \right) u_k u_{**} \\ &\quad + \rho u_k \frac{D u_{**}}{Da} + \rho u_{**} \frac{D u_k}{Da} - \tau \cdot \frac{\partial \hat{\mathbf{n}}}{\partial a} \cdot \hat{\mathbf{t}} \\ &\quad - \tau \cdot \hat{\mathbf{n}} \cdot \frac{\partial \hat{\mathbf{t}}}{\partial a} - \left[\left(\nabla \tau \cdot \frac{\partial \hat{\mathbf{X}}}{\partial a} \right) \cdot \hat{\mathbf{n}} \right] \cdot \hat{\mathbf{t}} \end{aligned} \tag{27}$$

with the material derivatives of the velocity scales given by :

$$\frac{Du_k}{Da} = u_k \left[\frac{C'_\mu}{4C_\mu} + \frac{1}{2k_w} \left(s_k + \nabla k \cdot \frac{\partial \hat{\mathbf{X}}}{\partial a} \right) \right] = u_k \left[\frac{C'_\mu}{4C_\mu} + \frac{1}{2} \left(s_\mathcal{K} + \nabla \mathcal{K} \cdot \frac{\partial \hat{\mathbf{X}}}{\partial a} \right) \right] \tag{28}$$

$$\begin{aligned} \frac{Du_{**}}{Da} = \frac{\kappa}{\ln(\frac{E\rho d u_k}{\mu})} \Bigg\{ & \frac{\kappa' u_t}{\kappa} + \left(\mathbf{s_u} + \nabla \mathbf{u} \cdot \frac{\partial \hat{\mathbf{X}}}{\partial a} \right) \cdot \hat{\mathbf{t}} + \mathbf{u} \cdot \frac{\partial \hat{\mathbf{t}}}{\partial a} \\ & - \frac{u_t}{\ln(\frac{E\rho d u_k}{\mu})} \left[\frac{E'}{E} + \frac{d'}{d} + \frac{1}{u_k} \frac{Du_k}{Da} + \frac{\left(\rho' + \nabla \rho \cdot \frac{\partial \hat{\mathbf{X}}}{\partial a} \right)}{\rho} - \frac{\left(\mu' + \nabla \mu \cdot \frac{\partial \hat{\mathbf{X}}}{\partial a} \right)}{\mu} \right] \Bigg\} \end{aligned} \tag{29}$$

Note that (27) is a mixed boundary condition since $\left(\frac{\partial \tau}{\partial a} \cdot \hat{\mathbf{n}} \right) \cdot \hat{\mathbf{t}}$ is related to $\mathbf{s_u} \cdot \hat{\mathbf{t}}$ through $\frac{Du_{**}}{Da}$. Note also that Eqs. (27) and (29) can be simplified in the particular case of incompressible flow since the spatial gradient of the density is always zero.

- flow sensitivity boundary condition in the normal direction :

$$\mathbf{s_u} \cdot \hat{\mathbf{n}} = - \left(\nabla \mathbf{u} \cdot \frac{\partial \hat{\mathbf{X}}}{\partial a} \right) \cdot \hat{\mathbf{n}} - \mathbf{u} \cdot \frac{\partial \hat{\mathbf{n}}}{\partial a} \tag{30}$$

- boundary condition for $s_\mathcal{K}$:

$$\begin{aligned} \left[\left(\mu' + \frac{\mu'_t}{\sigma_k} - \frac{\mu_t \sigma'_k}{\sigma_k^2} \right) \nabla \mathcal{K} + \left(\mu + \frac{\mu_t}{\sigma_k} \right) \nabla s_\mathcal{K} \right] \cdot \hat{\mathbf{n}} = & - \left[\nabla \mu \cdot \frac{\partial \hat{\mathbf{X}}}{\partial a} + \frac{\nabla \mu_t \cdot \frac{\partial \hat{\mathbf{X}}}{\partial a}}{\sigma_k} \right] \nabla \mathcal{K} \cdot \hat{\mathbf{n}} \\ & - \left(\mu + \frac{\mu_t}{\sigma_k} \right) \left[\nabla \mathcal{K} \cdot \frac{\partial \hat{\mathbf{n}}}{\partial a} + \nabla \left(\nabla \mathcal{K} \right) \cdot \frac{\partial \hat{\mathbf{X}}}{\partial a} \cdot \hat{\mathbf{n}} \right] \end{aligned} \tag{31}$$

- boundary condition for $s_\mathcal{E}$:

$$s_\mathcal{E} = \frac{3}{u_k} \frac{Du_k}{Da} - \frac{\kappa'}{\kappa} - \frac{d'}{d} - \nabla \mathcal{E} \cdot \frac{\partial \hat{\mathbf{X}}}{\partial a} \tag{32}$$

3 Finite element formulation and adaptive remeshing

The RANS equations and the logarithmic form of the turbulence equations are solved by a finite element method. The velocity and the logarithmic turbulence variables are discretized using 6-noded quadratic elements. Fluid pressure is discretized by piecewise linear continuous functions (Taylor-Hood element). For high Reynolds number, the equations are dominated by convection and the standard Galerkin discretization may lead to non-physical oscillations and convergence difficulties. Hence, some form of upwinding is required. This is done by using the Streamline Upwind/Petrov-Galerkin (SUPG) stabilized formulation initially proposed by Brooks and Hughes [18] and further improved by Ilinca *et al.* [19]. The discretization of the equations leads to a system of non-linear algebraic equations which are linearized by Newton's method. All linear algebraic systems are solved using a sparse direct solver.

The accuracy of the finite-element approximation is directly related to the local mesh size (see Refs. [20, 21]). An adaptive remeshing procedure is employed to improve the accuracy, by refining the mesh in regions of high error in the flow and sensitivity variables. Regions targeted for refinement are identified by the so-called Zhu-Zienkiewicz (ZZ) error estimator [22, 23] which evaluates estimates in elemental error norms. The ZZ error estimator belongs to the family of post-processing techniques (or least-squares-based recovery techniques) [5, 24]. These recovery-based estimators are very simple, yet they perform surprisingly well in practice if a proper norm of the error is used [25, 24, 26].

Error estimates are obtained by a local least-squares reconstruction of the solution derivatives for the velocity and pressure field and the logarithms of turbulence variables. Note that, an error estimate for the eddy viscosity is also constructed since slowly varying fields of $\mathcal{K}$ and $\mathcal{E}$ may result in rapid variation of μ_t.
Once error estimates are obtained for all variables (flow and sensitivities), an optimal mesh size distribution is determined using the asymptotic convergence rate of the finite-element method and the principle of equidistribution of the error [21] : the optimal mesh is generated to redistribute the mesh sizes so that each element has the same contribution to the norm of the total error. This is performed in an iterative fashion, beginning with a coarse mesh and producing a sequence of meshes which reduce the error by a constant factor over that of the previous mesh. The mesh characteristics (element size) are derived separately for each dependent variable. Note that refining on both the flow and its sensitivities is of crucial importance in the present context. Indeed, the flow variables and their sensitivities do not exhibit rapid variations at the same locations (and each sensitivity has its own area of rapid variations). Consequently, the region of high errors on a given mesh are generally not the same for all flow variables and all sensitivity variables. Thus, to compute accurate solutions for all variables, we calculate and drive the adaptive process with as many error estimates as there are dependent variables involved in the problem at hand. The minimum element size predicted by all the dependent variables is selected on a given element. The computational domain is then remeshed using an advancing front technique. Details of this adaptive remeshing procedure may be found in the literature [20, 21, 27, 26].

4 Adaptive Code Verification by the Method of the Manufactured Solution

4.1 Definition of the problem

In this section, we use the Method of the Manufactured Solution for Code Verification. The manufactured solution mimics the near-wall behavior of a two-dimensional, steady incompressible turbulent boundary-layer. The near-wall behavior of all the specified quantities is similar to what is observed in near-wall turbulent flows. The Reynolds number is set to one million. The manufactured solution and the source terms defining the modified problem are described in details in Refs. [28, 29]. Additional source terms are required for verification of wall functions; see details in Ref. [30]. Here, we extend the manufactured solution to verify wall functions for sensitivity analysis for shape parameters. We focus on sensitivity of the flow response with respect to the vertical position of the flat wall along which the turbulent boundary-layer is developing. The problem is illustrated in Figure 1 where y_0 is the shape parameter of interest. For completeness, we

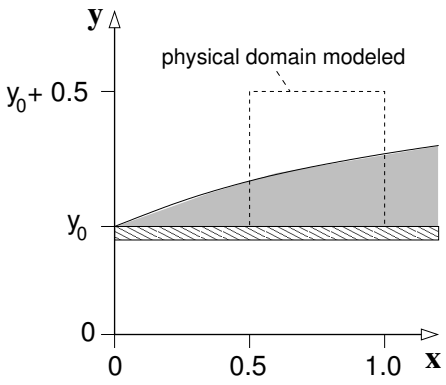

Figure 1: Manufactured problem: computational domain

briefly describe the manufactured flow and sensitivity fields. As illustrated in Figure 1, the physical domain is a square of side $0.5L$ with $0.5L \leq x \leq L$ and $0 \leq y - y_0 \leq 0.5L$. The Reynolds number Re is defined by $Re = \frac{U_1 L}{\nu}$ where U_1 is the reference velocity, L the reference length and ν the kinematic viscosity. All quantities presented below are non-dimensional using L and U_1 as the reference length and velocity scale.

In the definition of the velocity components and pressure coefficient we will use the following *similarity variable* with $\sigma = 4.$ and $\sigma_\nu = 2.5\sigma$:

$$\eta = \frac{\sigma(y - y_0)}{x} \quad ; \quad \eta_\nu = \frac{\sigma_\nu(y - y_0)}{x} \tag{33}$$

The velocity component in the x direction, u, is given by

$$u = \text{erf}(\eta) \tag{34}$$

The velocity component in the y direction, v, is given by

$$v = \frac{1}{\sigma\sqrt{\pi}}\left(1 - e^{-\eta^2}\right) \tag{35}$$

and the pressure is taken to be :

$$p = 0.5\ln\left(2x - x^2 + 0.25\right)\ln\left(4y^3 - 3y^2 + 1.25\right) \tag{36}$$

The manufactured field of k for the MS is generated using the following equation with $k_{max} = 0.01$:

$$k = k_{max}\eta_\nu^2 e^{1-\eta_\nu^2} + \alpha_k \tag{37}$$

The dissipation rate ϵ is as follows with $\nu_{max} = 0.001$:

$$\epsilon = 0.36\frac{k_{max}^2}{\nu_{max}}e^{-\eta_\nu^2} + \alpha_\epsilon \tag{38}$$

Finally, the eddy-viscosity is obtained from

$$\nu_t = c_\mu\frac{k^2}{\epsilon} \tag{39}$$

We have added small constants α_k and α_ϵ to the MS Fields for k and ϵ compared to what is described in Ref. [28] to avoid logarithms of zero values. Recall that the computational variables for the turbulence model are the logarithms of k and ϵ. See Ref. [26] for details.

$$\alpha_k = 10^{-5} \quad ; \quad \alpha_\epsilon = 10^{-3} \tag{40}$$

The analytical solution for all variables is imposed on the inflow and upper boundaries as Dirichlet boundary conditions. On the outlet, the normal and tangential forces on the boundary are imposed from the exact velocity and pressure fields. The diffusion fluxes of k and ϵ are also imposed from the exact solution. Hence, on the outlet Neumann boundary conditions are applied on all variables. On the wall (bottom boundary), the type of boundary conditions are determined by the wall functions (see Section 2.1.2) :

- u : Robin boundary condition
- k : Neumann boundary condition
- v : Dirichlet boundary condition
- ϵ : Dirichlet boundary condition

As described in Ref. [30], source terms are added in the standard wall functions boundary conditions to ensure compatibility with the manufactured solution. The wall distance is set to $d = 0.006$ to ensure, for a Reynolds number of one million, that the non-dimensional wall distance d^+ Eq. (11) lies in $[30, 300]$ on all walls remaining as close as possible to 30 for improved accuracy.

Direct differentiation of the manufactured solution with respect to y_0 yields the following expressions for

the sensitivities of the flow and turbulence variables :

$$
\begin{aligned}
S_u &= -\frac{2\sigma}{x\sqrt{\pi}} e^{-\eta^2} \\
S_v &= -\frac{2\eta}{x\sqrt{\pi}} e^{-\eta^2} \\
S_p &= \frac{3(y-yo)[1-2(y-yo)]}{4(y-yo)^3 - 3(y-yo)^2 + 1.25} \log(2x - x^2 + 0.25) \\
S_k &= \frac{2k_{max}\sigma_\nu}{x} \eta_\nu (\eta_\nu^2 - 1) e^{(1-\eta_\nu^2)} \\
S_\epsilon &= \frac{0.72 k_{max}^2 \sigma_\nu}{x \nu_{max}} \eta_\nu e^{-\eta_\nu^2}
\end{aligned}
$$

The boundary conditions for the sensitivity problem are deduced from the corresponding flow boundary conditions described above (see Section 2.2.2 for more details).

4.2 Verification of flow and sensitivity solutions

The flow and sensitivity fields are solved using the adaptive finite-element method. On parameter dependent boundary curves, boundary conditions for the sensitivity problem are computed using the technique proposed by Duvigneau and Pelletier [31]. It consists in a least-squares reconstruction, using Taylor series as basis functions, that is constrained to satisfy the flow boundary conditions. The least-squares problem is defined over patches of 8 layers of neighboring elements and uses Taylor expansion of degree 6. The methodology has been presented in Ref. [31] for laminar flows and is extended here for turbulent flows with wall functions. It will be shown that it ensures a sufficiently accurate evaluation of transpiration terms in the sensitivity boundary conditions.

All flow and sensitivity variables contribute to the error estimation so that the mesh adaptation process is driven by 10 error estimates (velocity, pressure, k, ϵ and μ_t and their corresponding sensitivities). Eight grid adaptation cycles have been performed. Figure 2 shows the final mesh containing 123 689 nodes. It is typical of adapted meshes for boundary layer flow problems as expected. Extensive refinement is observed in the near-wall region. Several bands of refinement can also be identified which correspond to regions of rapid variation in velocity, $\mathcal{K}$, $\mathcal{E}$ and μ_t and their sensitivities.

Figure 3 presents the trajectories of true and estimated error norms for the flow variables and their sensitivities. The norms showed are the following :

$$
\begin{aligned}
\text{H1U} &: ||\mathbf{u}||_{H^1} = \sqrt{\int_\Omega (\nabla u \cdot \nabla u + \nabla v \cdot \nabla v)\ d\Omega} \\
\text{H1P} &: ||p||_{H^1} = \sqrt{\int_\Omega \nabla p \cdot \nabla p\, d\Omega} \\
\text{EVM} &: ||\mu_t||_{eqv} = \sqrt{\int_\Omega \nabla \mu_t \cdot \nabla \mu_t\, d\Omega}
\end{aligned}
$$

As can be seen, errors on both the flow and the sensitivities decrease from cycle to cycle. The trajectory of the error estimators converges to that of the true error with mesh adaption. This property (asymptotic exactness) implies that accuracy and reliability improve with mesh refinement.

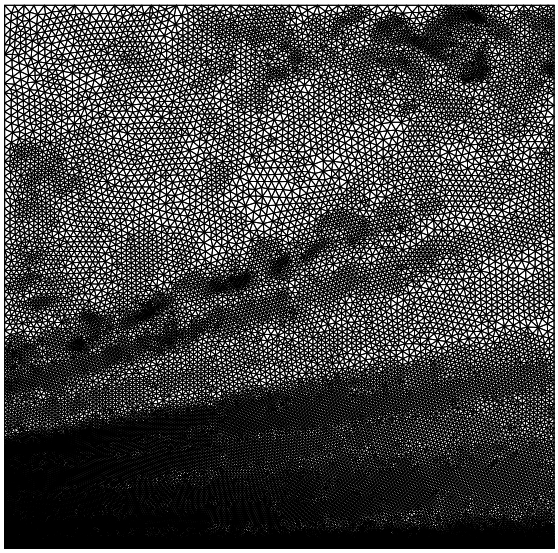

Figure 2: Manufactured solution : Final adapted mesh

4.3 Verification for integrals of surface quantities and their sensitivities

We now turn our attention to the evaluation the friction resistance R_f on the wall and its sensitivity, two integral quantities. Taking $\rho U_{\text{ref}}^2 L_{\text{ref}}$ as a reference force, the friction resistance is computed as follows :

$$R_f = \frac{1}{\rho U_{\text{ref}}^2 L_{\text{ref}}} \int_{\Gamma_w} \tau \cdot \hat{\mathbf{n}} \cdot \hat{\mathbf{t}} \, d\Gamma = \int_{\Gamma_w} \left[(\mu + \mu_t)(\frac{\partial u}{\partial y} + \frac{\partial v}{\partial x}) \right] \, d\Gamma$$

The last integral is a simplified expression for our particular case using $\hat{n} = [0,1]^T; \hat{t} = [1,0]^T$.

Direct differentiation of the above expression yields the sensitivity of the friction coefficient which is an Eulerian derivative in the parameter space. Using the following derivatives of the geometric quantities :

$$\frac{\partial \hat{n}}{\partial y_0} = \frac{\partial \hat{t}}{\partial y_0} = [0,0]^T \qquad ; \qquad \frac{\partial \hat{X}}{\partial y_0} = [0,1]^T \tag{41}$$

leads to the following simplified expression for the Eulerian sensitivity of the friction resistance :

$$\frac{\partial R_f}{\partial y_0} = \int_{\Gamma_w} \left[(\mu + \mu_t)(\frac{\partial S_u}{\partial y} + \frac{\partial S_v}{\partial x}) + S_{\mu_t}(\frac{\partial u}{\partial y} + \frac{\partial v}{\partial x}) \right] \, d\Gamma \tag{42}$$

The required Lagrangian sensitivity is easily derived using the material derivative in parameter space. In our particular case, the expression simplifies to :

$$\begin{aligned}
\frac{dR_f}{dy_0} =& \frac{1}{\rho U_{\text{ref}}^2 L_{\text{ref}}} \int_{\Gamma_w} \frac{d\tau}{dy_0} \cdot \hat{\mathbf{n}} \cdot \hat{\mathbf{t}} \, d\Gamma \\
=& \frac{1}{\rho U_{\text{ref}}^2 L_{\text{ref}}} \int_{\Gamma_w} \left(\frac{\partial \tau}{\partial y_0} + \nabla \tau \cdot \frac{\partial \hat{X}}{\partial y_0} \right) \cdot \hat{\mathbf{n}} \cdot \hat{\mathbf{t}} \, d\Gamma \\
=& \frac{\partial R_f}{\partial y_0} + \frac{1}{\rho U_{\text{ref}}^2 L_{\text{ref}}} \int_{\Gamma_w} \nabla \tau \cdot \frac{\partial \hat{X}}{\partial y_0} \cdot \hat{\mathbf{n}} \cdot \hat{\mathbf{t}} \, d\Gamma \\
=& \frac{\partial R_f}{\partial y_0} + \frac{1}{\rho U_{\text{ref}}^2 L_{\text{ref}}} \int_{\Gamma_w} [(\mu + \mu_t)(\frac{\partial^2 u}{\partial y^2} + \frac{\partial^2 v}{\partial xy}) + S_{\mu_t}(\frac{\partial u}{\partial y} + \frac{\partial v}{\partial x})] \, d\Gamma
\end{aligned} \tag{43}$$

As can be seen, the Lagrangian sensitivity is equal to the Eulerian sensitivity plus a transpiration term (last term on the third and fourth lines) which accounts for the change in the position of the wall boundary caused

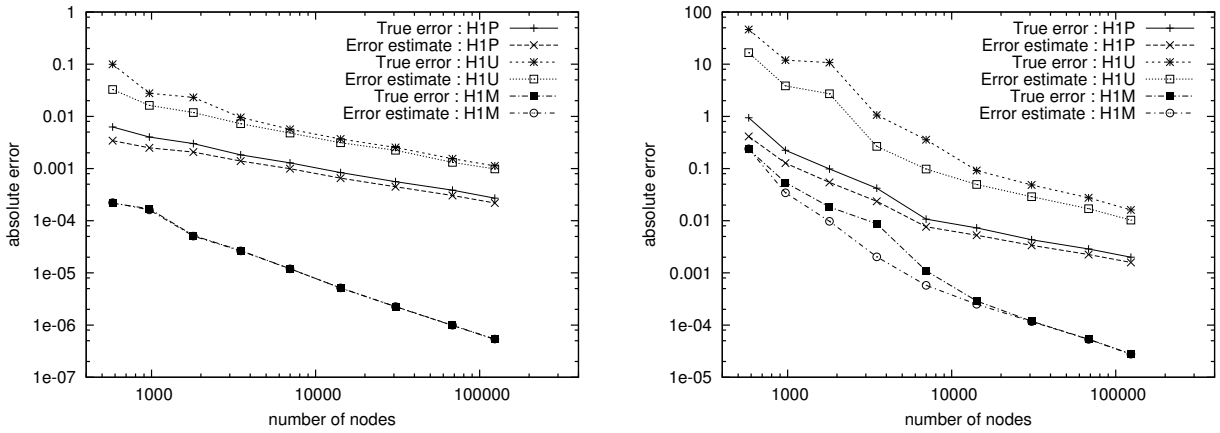

(a) Flow

(b) Sensitivity

Figure 3: Manufactured solution : Trajectories of true and estimated error norms

by changes in the parameter y_0. Since the wall boundary condition does not depend on y_0, its Lagrangian derivative is zero. This is confirmed by Table 2 which gives the exact value of the Friction Coefficient and its sensitivities. This means that the transpiration term (last term on the fourth line in Eq. (43)) exactly cancels out the Eulerian sensitivity given by Eq. (42). This can easily be seen since $\frac{\partial .}{\partial y} = -\frac{\partial .}{\partial y_0}$.

Figure 4 shows the evolution of the true errors in R_f and its sensitivities with adaptive cycles. As can

Exact Friction Coefficient	Exact Eulerian sensitivity	Exact Lagrangian sensitivity
$R_f = 0.354686\,10^{-5}$	$\frac{\partial R_f}{\partial y_0} = -0.267451\,10^{-3}$	$\frac{dR_f}{dy_0} = 0$

Table 2: Manufactured solution : Friction resistance

be seen, the errors decrease from cycle to cycle. Hence, the errors on the gradient of integral forces can be reduced as much as desired using the adaptive process. The proposed methodology for computing the gradient of integral forces is thus verified as well as the expressions for the transpiration terms.

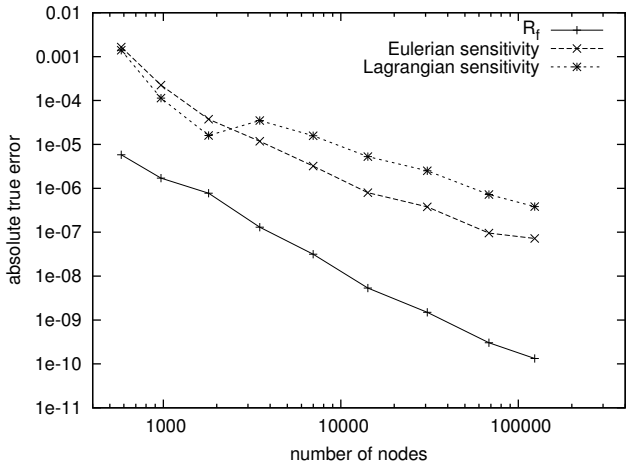

Figure 4: Grid convergence of the sensitivities of the friction resistance on the wall

4.4 Verification of pointwise error estimates

Finally, the accuracy of the error estimation technique for point values of flow solution is examined. The ZZ reconstruction recovers only the solution derivatives not its value. It can not be used for pointwise error estimates of the solution itself. To do this, we use a higher order element based least-squares reconstruction as descibed in Ref. [32]. The coordinates of the three local points under consideration are : Point 1 (0.600,0.001), Point 2 (0.750,0.002) and Point 3 (0.900,0.200). At these locations, we study the values of the non-dimensional velocity components (U and V), the pressure coefficient C_p, the non-dimensional eddy-viscosity μ_t and their associated errors. Note that here, the pressure coefficient is defined as :

$$C_p = \frac{p}{\rho U_{\text{ref}}^2} \tag{44}$$

The results are collected in table 3. All values have been checked for grid convergence with a convergence

Local point	Variables	Value	True Error	Estimated Error	Efficiency index
1	U	$0.752228\,10^{-2}$	$0.138221\,10^{-6}$	$0.100532\,10^{-6}$	0.727
	V	$0.626501\,10^{-5}$	$0.362070\,10^{-8}$	$0.149948\,10^{-7}$	4.141
	C_p	$0.961490\,10^{-2}$	$0.100520\,10^{-8}$	$0.386091\,10^{-8}$	3.841
	μ_t	$0.748136\,10^{-9}$	$0.114963\,10^{-11}$	$0.778382\,10^{-12}$	0.677
2	U	$0.120354\,10^{-1}$	$0.229121\,10^{-6}$	$0.167990\,10^{-6}$	0.733
	V	$0.159042\,10^{-4}$	$0.142939\,10^{-6}$	$0.116034\,10^{-6}$	0.812
	C_p	$0.191728\,10^{-1}$	$0.145184\,10^{-7}$	$0.790371\,10^{-8}$	0.544
	μ_t	$0.209155\,10^{-8}$	$0.432803\,10^{-12}$	$0.676875\,10^{-12}$	1.564
3	U	$0.791275\,10^{+0}$	$0.358949\,10^{-6}$	$0.903074\,10^{-7}$	0.252
	V	$0.770422\,10^{-1}$	$0.538351\,10^{-6}$	$0.628828\,10^{-6}$	1.168
	C_p	$0.161486\,10^{-1}$	$0.131497\,10^{-6}$	$0.310776\,10^{-6}$	2.363
	μ_t	$0.676005\,10^{-4}$	$0.111044\,10^{-9}$	$0.189889\,10^{-8}$	17.100

Table 3: Results for local flow quantities

behaviour similar to the one observed for the friction resistance (see figure 4). The largest value of the true relative error occurs for μ_t at point 1 ($0.15366591\,10^{-2}$). In general the finite element solution reproduces the exact solution with more than four or five significant digits. The element based error estimator predicts no more than the order of magnitude of the true error for all variables at the three locations except for μ_t at point 3. Deriving an average efficiency index is a non-trivial task. Simple arithmetic averaging can lead to misleading results. We have opted to normalize all efficiency indices by using their inverse when they are greater than one. This is acceptable since an index value of ξ is equivalent to one of $\frac{1}{\xi}$ the difference being that one of them indicates overestimation while the other one expresses underestimation; neither being preferable. This leads to a mean efficiency index of 0.498. These results are satisfactory in terms of accurate error prediction for this class of problem and are typical of what was observed previously. However, since the error is not fully reproduced, it would be useful and desirable to develop safety factors to compute error bands in the spirit of the Grid Convergence Index [5]. Finding the safety factors would require a large number of test cases for achieving error bands that are correct in ninety five percent of the cases. The present results are promising and bode well for deriving a single-grid error banding procedure. In light of these results, we can confidently state that the adaptive finite element flow and sensitivity solver is verified.

5 Solution Verification with mesh adaptation

Now that the flow solver, the adaptive procedure and the error estimators have been verified, we turn our attention to the flow over a backward facing-step to illustrate the concept of Solution Verification. The

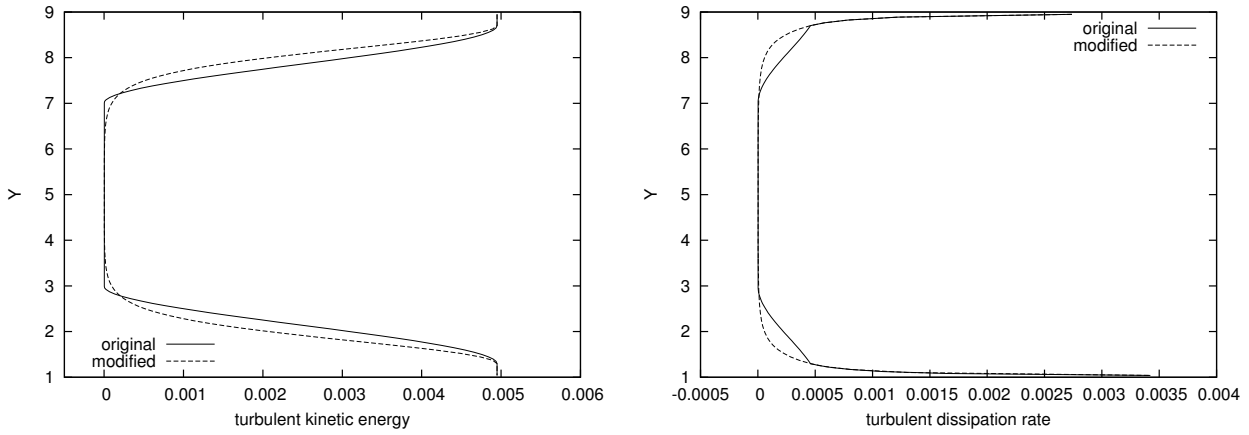

(a) Inlet profiles for k

(b) Inlet profiles for ϵ

Figure 5: Inlet profiles for the turbulence variables

configuration corresponds to the ERCOFTAC test case C-30 for which the Reynolds number based on the step height is 50000. This configuration was used in the two Workshops on CFD Uncertainty Analysis and details on the inlet profiles can be found in Ref. [33].

The boundary conditions along walls are prescribed using wall functions. At the inlet, Dirichlet boundary conditions are applied and at the outlet we prescribed homogeneous Neumann boundary conditions. The inlet profiles for all variables are defined by fitting mathematical expressions to experimental data so as to ensure the continuity of both the variables and their derivatives. The original inlet profiles for the turbulent variables are plotted as solid lines in figure 5. As stated, these profiles are constructed in a piecewise manner to obtain C^1 continuous functions as required by most numerical techniques. However, the logarithms of these C^1 continuous functions are not necessarily C^1 continuous. This may lead to numerical problems for our code. Hence, we sightly modified the inlet profiles. The background experimental data are unchanged but the piecewise mathematical treatment for obtaining the profiles is done so that our computational variables (the logarithms of the turbulent variables) is C^1 continuous. The resulting inlet profiles thus obtained are plotted as dashed lines in figure 5. We believe that the modification of the profiles will only have minor influence on the computed solution since the physic behind these two sets of profiles remains the same. Only, the mathematical assembly is different.

Solutions are considered mesh independent when no major changes occur with further mesh refinement. Seven grid adaptation cycles have been performed. Figure 6 shows the last adapted grid which contain 55 776 nodes. A close-up view of the adapted mesh around the step corner is also provided in figure 7. It is similar to adapted meshes obtained previously for simulations of the flows over the backward facing step experimental configurations of Kim [34] and of Vogel *et al.* [35]. Again, a high degree of refinement has occured intensively in the near-wall region. Different bands of refinement can also be identified which correspond to regions of rapid variation in velocity, $\mathcal{K}$, $\mathcal{E}$ and μ_t.

Before proceeding with any analysis of the results, we must check that the non-dimensional wall distance chosen for each wall lies in the interval of validity imposed by the wall functions which requires that $y+$ is less than 300 and greater than 30 but preferably as close to 30 as possible. Figure 8 gives the evolution of $y+$ with adaptive cycles for each wall. As can be seen, the wall distances converge with the adaptive cycles. And, for the last adapted grid, the above condition is satisfied everywhere except near the corner singularity.

We first examine the result for the recirculation length. Figure 9 shows the evolution of the computed recirculation length with adaptive cycles. As can be seen, convergence is achieved. The value of the non-dimensional recirculation length computed on the last adapted mesh is estimated at 5.446699. The evaluation of the discretization error is evaluated to 0.102065. Thus, we report that $L_{\text{rec}}/D = 5.4 \pm 0.1$.

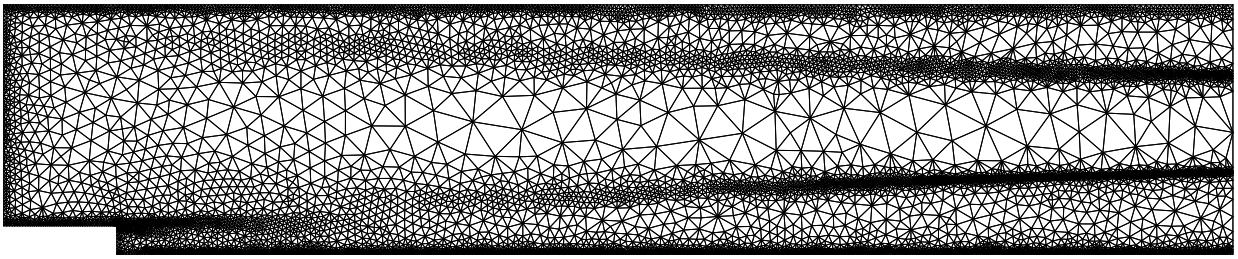

Figure 6: Adapted mesh for the backward facing step

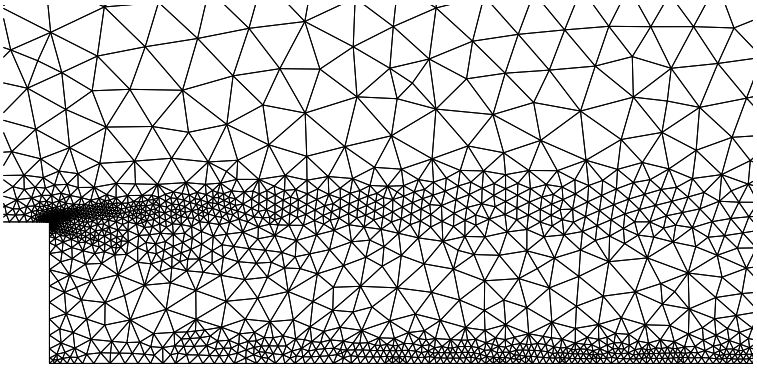

Figure 7: Inside view of the adapted mesh around the step

We now examine several integral quantities : the friction resistance R_f on the bottom and top walls and the pressure resistance R_p on the bottom wall. Taking $\rho U_{\text{ref}}^2 L_{\text{ref}}$ as a reference force, the friction resistance is computed from Eq. (4.3) and the pressure resistance as follows :

$$R_p = \frac{1}{\rho U_{\text{ref}}^2 L_{\text{ref}}} \int_{\Gamma_w} -(p - p_{\text{outlet}}) \hat{\mathbf{n}} \cdot \mathbf{e_y} \, \mathbf{d\Gamma} \tag{45}$$

Table 4 gives the numerical values of the coefficients and their estimated errors on the last adaptive grid.

	R_f on the bottom wall	R_f on the top wall	R_p on the bottom wall
Value	$0.526499\,10^{-01}$	$0.672544\,10^{-01}$	$0.119342\,10^{+00}$
Estimated Error	$0.993600\,10^{-02}$	$0.253363\,10^{-01}$	$0.223481\,10^{-01}$

Table 4: Results for the resistance coefficients

Finally, the errors on pointwise flow quantities are examined. The non-dimensional coordinates of the three points under consideration are : Point 1 (0.0,1.1), Point 2 (1.0,0.1) and Point 3 (4.0,0.1). At these locations, we consider the values of the velocity components (U and V), the pressure coefficient C_p, the eddy-viscosity μ_t and their errors. Note that here, the pressure coefficient is defined as :

$$C_p = \frac{p - p_{\text{outlet}}}{1/2 \rho U_{\text{ref}}^2}$$

The results are collected in table 5. All values have been checked for grid convergence with a convergence behaviour similar to the one observed for the recirculation length (see figure 9). The maximum estimated

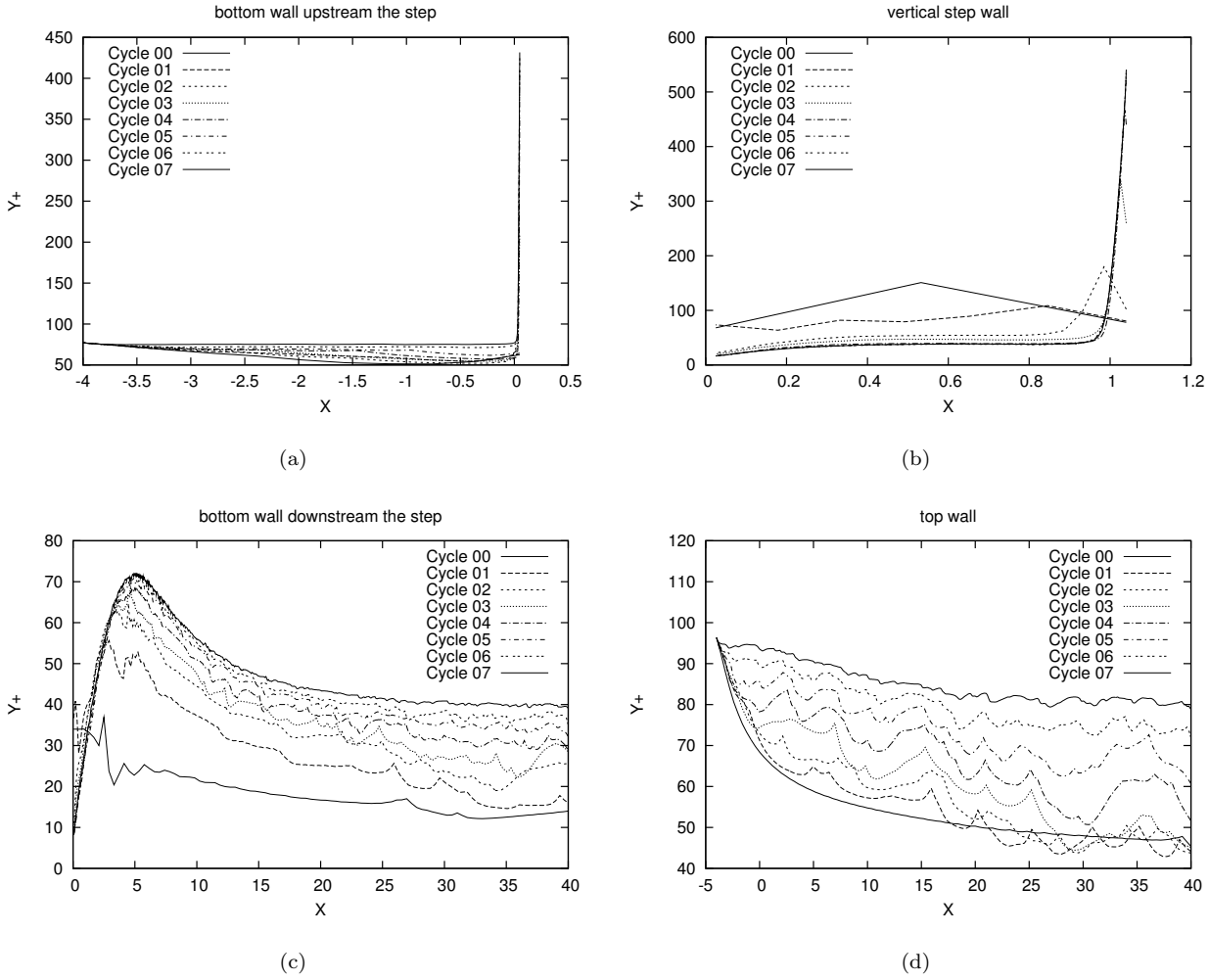

Figure 8: Evolution of $y+$ with adaptive cycles

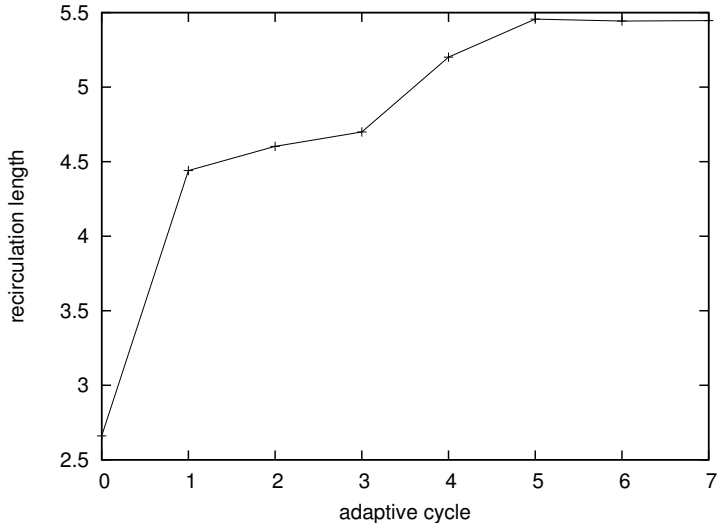

Figure 9: Evolution of recirculation length with adaptive cycles

Local point	Variables	Value	Estimated Error
1	U	$+0.647700\,10^{+00}$	$0.396496\,10^{-04}$
	V	$+0.289958\,10^{-01}$	$0.102193\,10^{-03}$
	C_p	$-0.133953\,10^{+00}$	$0.339351\,10^{-04}$
	μ_t	$+0.171898\,10^{-02}$	$0.314743\,10^{-06}$
2	U	$-0.944773\,10^{-01}$	$0.371167\,10^{-04}$
	V	$+0.721732\,10^{-02}$	$0.110560\,10^{-04}$
	C_p	$-0.237365\,10^{+00}$	$0.226732\,10^{-05}$
	μ_t	$+0.195559\,10^{-02}$	$0.175705\,10^{-04}$
3	U	$-0.125582\,10^{+00}$	$0.109521\,10^{-04}$
	V	$-0.608819\,10^{-02}$	$0.796328\,10^{-06}$
	C_p	$-0.139171\,10^{+00}$	$0.484284\,10^{-05}$
	μ_t	$+0.612614\,10^{-02}$	$0.185213\,10^{-04}$

Table 5: Results for local flow quantities

relative error occurs for μ_t at point 2 ($0.898476\,10^{-2}$). Generally speaking the error estimates appear sharp in that they are small enough to provide hints that we have achieved 4 to 5 significant digits of accuracy in predictions.

6 Validation and Uncertainty analysis of CFD results

6.1 Definition of the problem

We now consider the flow of air around a square cross-section cylinder in the proximity of a solid wall as investigated by Wu and Martinuzzi using Laser Doppler Velocimetry [10]. The experimental configuration consists of a smooth flat plate located in the 0.45 m $\times$ 0.45 m test section of a suction-type wind tunnel. Details of the experimental set-up are shown in Figure 10. Experiments were conducted for a Reynolds

number of 22000 based on D, the dimension of the side of the square obstacle, and U_0, the inlet velocity. The oncoming free stream turbulence intensity is set at 1% and the mean flow is steady. In the reminder of

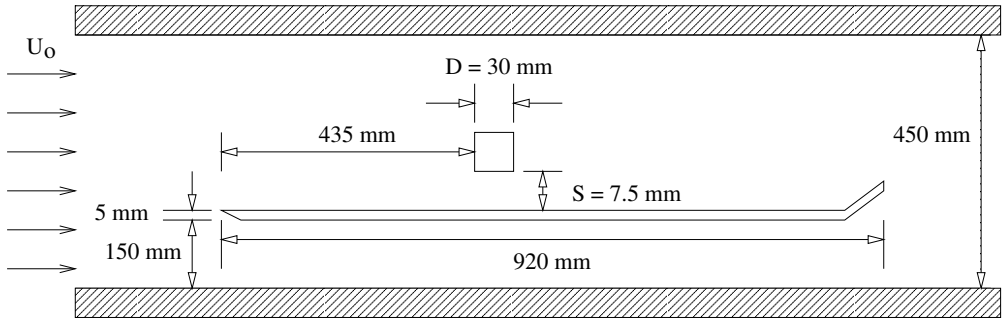

Figure 10: Experimental Set-up

the article, all quantities presented are non-dimensional using D and U_0 as the reference length and velocity scale.

6.2 Computational domain and sensitivity analysis

The computational domain and boundary conditions are shown in Figure 11. In the experiment, an end-plate flap was adjusted to maintain parallel flow below the plate. However, it is generally accepted that the flow above the plate is not influenced by the flow under the plate. Hence, only the portion of the tunnel located above the plate is included in the computational model. Also it was deemed unnecessary to simulate the effect of the end-plate flap.

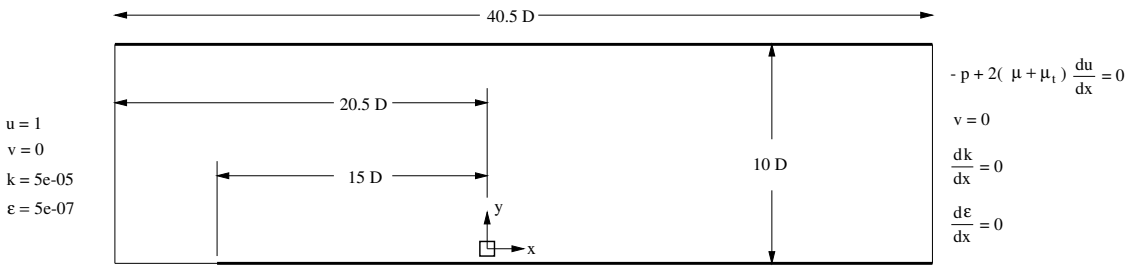

Figure 11: Computational domain and boundary conditions

Wall functions provide boundary conditions along the upper wall of the tunnel, the sides of the obstacle, and the plate. As was shown in a previous study [35], it is necessary to include the thickness of the real plate in the computational model in order to reproduce the physically observed stagnation point at the leading edge of the plate. The half-thickness of the plate model is set to 0.083. With this model geometry, the production of k, which depends on the velocity gradients, is triggered a short distance upstream of the leading edge of the plate so that realistic levels of turbulence are reproduced in this region. The leading edge of the plate, as well as the corners of the cylinder, are rounded to avoid corner singularities with wall functions.

The inlet value of k is set to achieve an inflow with a turbulence intensity of 1%. Based on previous experience [35], the inlet value of ϵ is adjusted so that the inlet eddy-viscosity is equal to ten times the molecular viscosity.

The baseline configuration is obtained for $S = S_0 = 0.25$. We use shape sensitivity analysis to look at the effects of uncertainties in the gap size S between the square cylinder and the flat plate. The required sensitivities of geometric quantities are given by :

$$\frac{\partial \hat{\mathbf{n}}}{\partial S} = \frac{\partial \hat{\mathbf{t}}}{\partial S} = [0,0]^T \quad ; \quad \frac{\partial \hat{\mathbf{X}}}{\partial S} = [0,-1]^T$$

6.3 Numerical results

Mesh independent flow and sensitivity solutions are obtained by the adaptive remeshing procedure. The final mesh, after 8 adaptive remeshings, has 556,567 nodes. Figure 12 and 13 show the 6^{th} mesh generated by the adaptive process (the 8^{th} mesh being too fine to be of any visual interest once displayed in a figure). The refinement in the boundary layers, shear layers and near the surface of the obstacle, can clearly be seen.

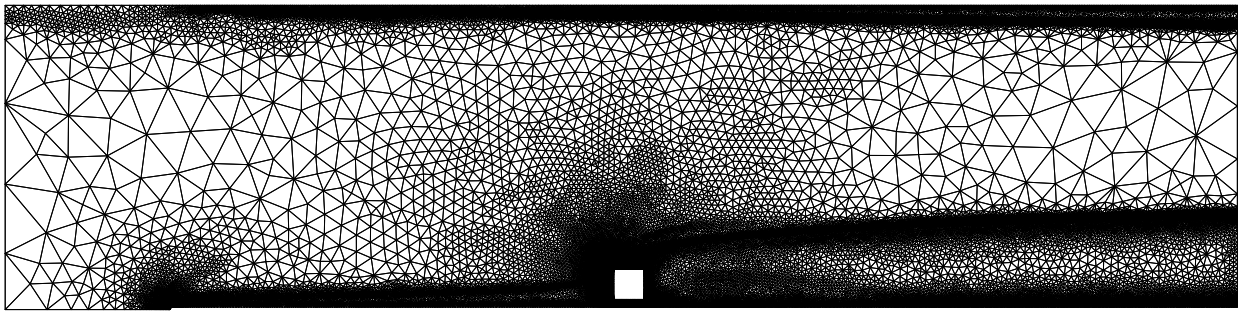

Figure 12: Mesh after 6 cycles of adaption

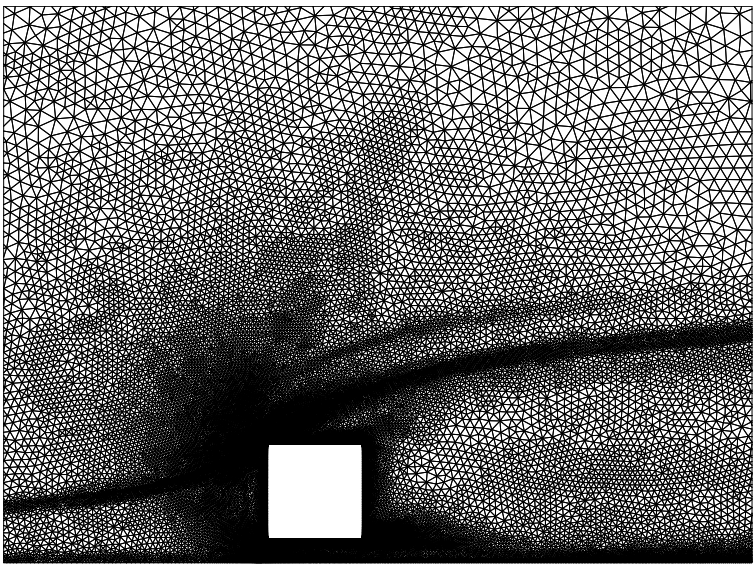

Figure 13: Mesh after 6 cycles of adaption near obstacle

Figure 14 shows the distribution of the non-dimensional distance to the wall, as defined by Eq. (11), along the flat plate with adaptive cycles. As can be seen, mesh independent boundary conditions are achieved and all values of y^+ satisfy the condition $30 < y^+ < 300$. This is indeed important to obtain a proper modelization of the flow with wall functions. Although not illustrated here, similar observations hold for the distributions of y^+ along all wall boundaries.

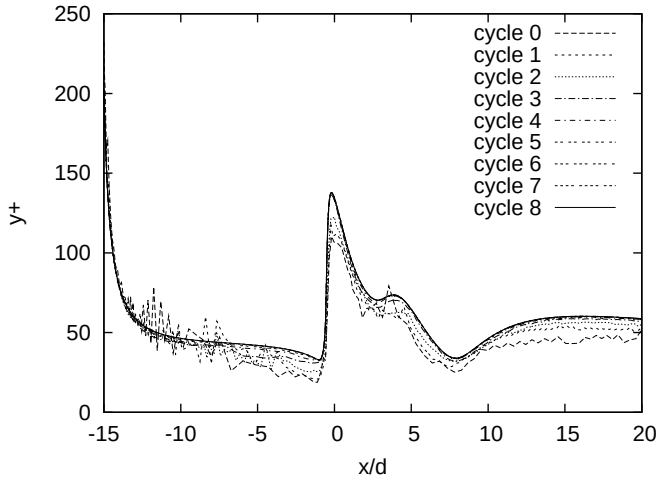

Figure 14: Distribution of y^+ along the plate with adaptive cycles

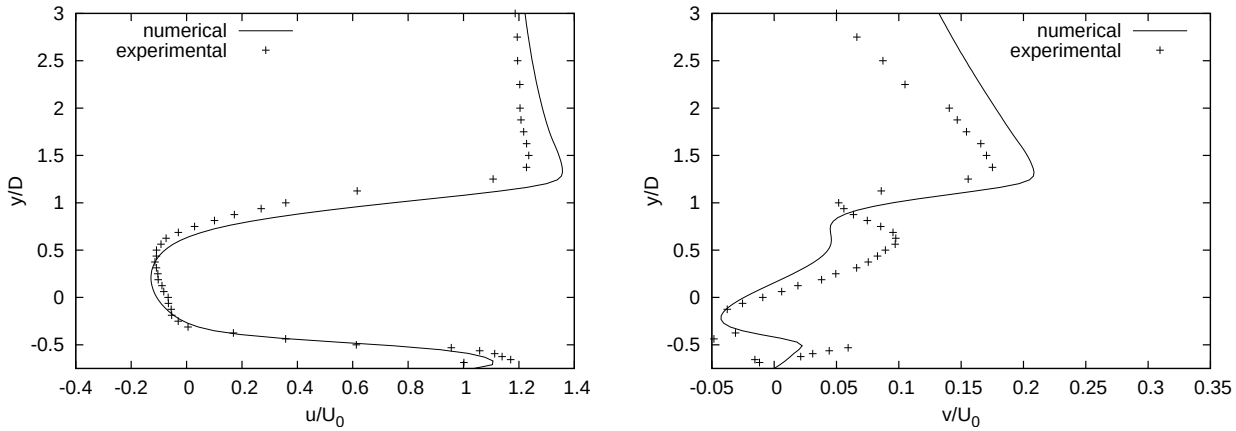

(a) streamwise component

(b) transverse component

Figure 15: Comparison of velocity profiles with experiments at $x = 1$

We now compare present flow predictions to the experimental data of Wu and Martinuzzi to illustrate Code Validation. Transverse profiles of the mean velocity components, u and v, and of the streamwise and shear components of the Reynolds stress, $-\overline{u'u'}$ and $-\overline{u'v'}$, are presented downstream of the cylinder at $x = 1$. The best prediction are obtained for u though the strength of the wall jet caused by the flow in the gap under the cylinder is slightly underpredicted. For the other quantities, the numerical results capture the major trends observed in the measurements but with some significant discrepancies in magnitude indicating that the turbulence model can not reproduce completely the flow physics.

We now perform uncertainty analysis on input data using sensitivity information. We consider uncertainties on the gap size and use lift and drag coefficients for illustrative purposes. We must consider the total derivatives of C_D and C_L since uncertainties in S cause the square to change its location. Thus, with $\sigma = \tau - pI$, we compute :

$$\frac{D}{DS}\begin{bmatrix} C_D \\ C_L \end{bmatrix} = \frac{1}{\rho U_0^2 L}\int_{\Gamma_w} \frac{\partial \sigma}{\partial S}\cdot \hat{\mathbf{n}}\, d\Gamma + \frac{1}{\rho U_0^2 L}\int_{\Gamma_w} \nabla\sigma \cdot \frac{\partial \hat{\mathbf{X}}}{\partial S}\cdot \hat{\mathbf{n}}\, d\Gamma \tag{46}$$

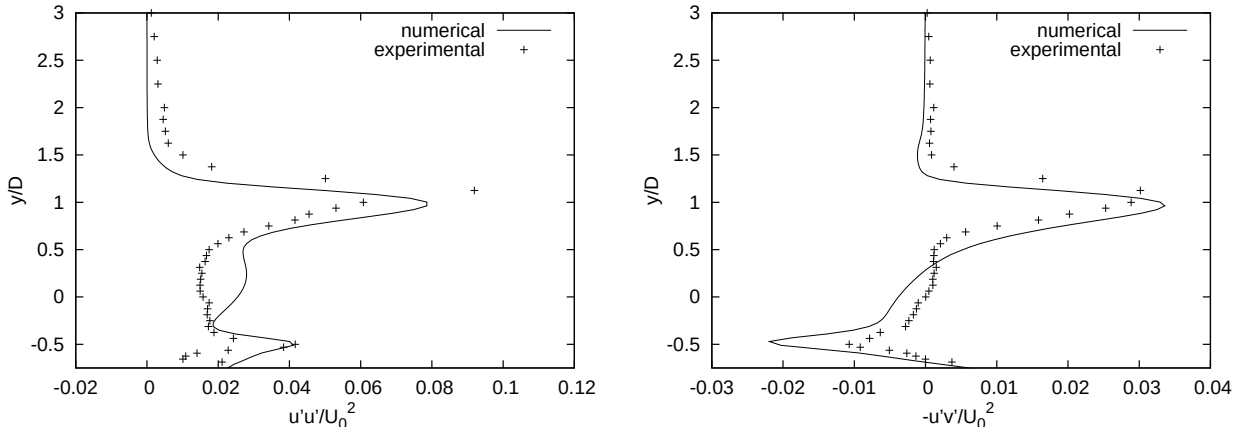

(a) streamwise normal component

(b) shear component

Figure 16: Comparison of Reynolds stress profiles with experiments at $x = 1$

(given that $\frac{\partial \hat{\mathbf{n}}}{\partial S} = \mathbf{0}$) to obtain the uncertainty estimates:

$$\delta C_D = \left| \frac{DC_D}{DS} \right| |\delta S|$$
$$\delta C_L = \left| \frac{DC_L}{DS} \right| |\delta S|$$

Table 6 shows the relative uncertainties on the outputs C_D and C_L due to various levels of uncertainty in the gap size $(1, 2, 3, 7\%)$. The data shows that uncertainty on the gap size causes modest uncertainties on the drag coefficient. However, the lift is marred with unacceptably large uncertainty estimates : 1% on S causes an uncertainty of 7.465% while an input uncertainty of 3% causes an output uncertainty of 22%, indicating that we have reached the limit of what is reasonable to do with first order sensitivity due to the highly non-linear dependency of the Lift with the gap size. However, another possibility might be that the numerical evaluation of transpiration terms in Eq. 46 are not fully grid converged in some areas.

$\frac{\delta S}{S_0}$	$\frac{\lvert\delta C_D\rvert}{C_D}$	$\frac{\lvert\delta C_L\rvert}{C_L}$
0.01	0.295%	7.465%
0.03	0.885%	22.395%
0.05	1.476%	37.325%
0.07	2.065%	52.255%

Table 6: Uncertainties on C_D and C_L

We now derive error bars on the friction coefficient along the flat plate due to uncertainties on the gap size value from :

$$\delta C_f = \pm \frac{\partial C_f}{\partial S} |\delta S|$$

Figure 17 shows the friction coefficient distribution with error bars corresponding to 1%, 3%, 5% and 7% of relative uncertainties on the gap size. As can be seen, the uncertainty on C_f is negligible for 1% in comparison to experimental uncertainties. However, it becomes significant for more than 3% of uncertainty

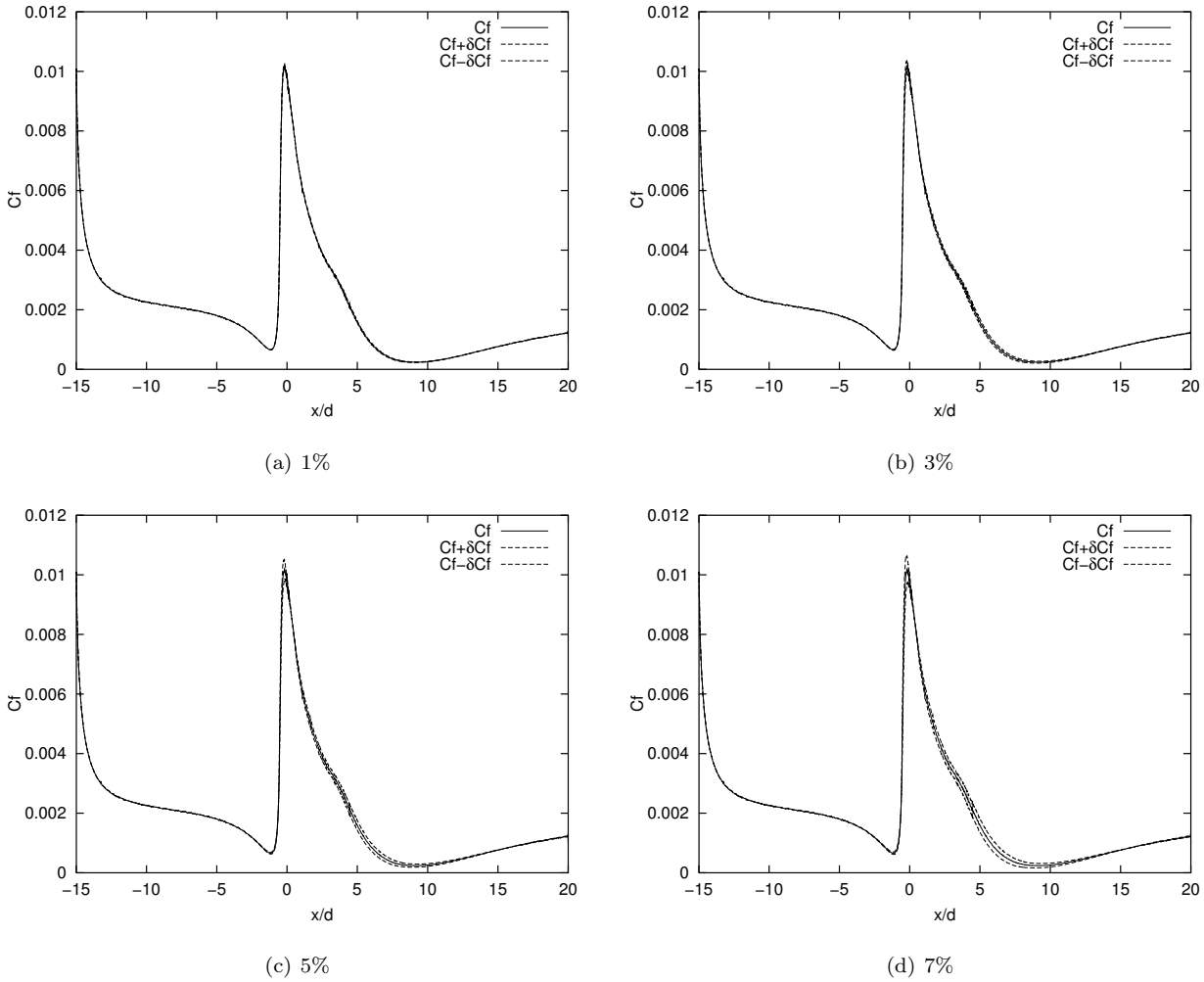

(a) 1%

(b) 3%

(c) 5%

(d) 7%

Figure 17: Error bars on the friction coefficient due to uncertainties on the gap size

on the gap size. For 7%, the uncertainty on the friction coefficient reaches values up to 10% of the nominal prediction in the area around the square cylinder.

7 Conclusions

This paper has presented Code Verification, Solution Verification and Validation results for an adaptive finite element RANSE solver. The flow solver, the adaptive procedure and the error estimator have all been verified in the context of k-epsilon models of turbulent flows with wall functions using the Method of the Manufactured Solution. This builds confidence in the numerical methods used and provides quantitative information about the accuracy and reliability of the error estimation procedures. Then, Solution Verification has been performed for two turbulent flows. Adaptivity has proven a very cost-effective tool for assessing and controlling numerical errors and obtaining grid independent results. A third step in the V&V process, Validation of the turbulent flow over a square cylinder in proximity of a flat plate has been presented using comparisons with experiments. Finally, Sensitivity Analysis of this complex problem has been performed to yield uncertainty estimates of physical quantities with respect to uncertainties in the gap size between the cylinder and the flat plate. We close by restating that our approach yields error estimates with a single grid computation. CGI based methods required a minimum of two grids if the convergence rate is assumed a priori and three if one prefers to estimate the effective convergence rate.

References

[1] In L. Eça and M. Hoekstra, editors, *1st Workshop on CFD Uncertainty Analysis*, Lisbon, Portugal, October 2004.

[2] In L. Eça and M. Hoekstra, editors, *2nd Workshop on CFD Uncertainty Analysis*, Lisbon, Portugal, October 2006.

[3] W. L. Oberkampf, F. G. Blottner, and D.P. Aeshliman. Methodology for computational fluid dynamics code verification and validation. In *AIAA 26th AIAA Fluid Dynamics Conferencet*, June 19-22, 1995 / San Diego, CA. AIAA Paper 95-2226.

[4] J.H. Ferziger and M. Perić. *Computational methods for fluid dynamics*. Springer Verlag, Berlin - New York, 2002. 3rd Edition.

[5] P. J. Roache. *Verification and Validation in Computational Science and Engineering*. Hermosa publishers, Albuquerque, NM, 1998.

[6] P. J. Roache. Code Verification by the Method of Manufactured Solutions. *ASME Journal of Fluids Engineering*, 114(1):4–10, 2002.

[7] P.J. Roache. Perspective : A method for uniform reporting of grid refinement studies. *Journal of Fluids Engineering, Transactions of the ASME*, 116:405–413, September 1994.

[8] I. Celik and O. Karatekin. Numerical experiments on application of Richardson extrapolation with nonuniform grids. *Journal of Fluids Engineering, Transactions of the ASME*, 119:584–590, September 1997.

[9] L. Eça and M. Hoekstra. An evaluation of Verification procedure for CFD applications. In *24th Symposium on Naval Hydrodynamics*, Fukuoka, Japan, 2002.

[10] K. Wu and R. Martinuzzi. Experimental study of the turbulent wake flow behind a square cylinder near a wall. In *ASME Fluids Engineering Division*, Vancouver, B.C., June 22-26 1997. No. FEDSM97-3151.

[11] T. Y. Chu and C. E. Hickox. Thermal convection with large viscosity variations in an enclosure with localized heating. *ASME Journal of Heat Transfer*, 112:388–395, 1990.

[12] F. Ilinca and D. Pelletier. Positivity preservation and adaptive solution for the $k-\epsilon$ model of turbulence. *AIAA Journal*, 36(1):44–51, 1998.

[13] B. E. Launder and J. Spalding. The numerical computation of turbulent flows. *Computer Methods in Applied Mechanics and Engineering*, pages 269–289, 1974.

[14] J.-P. Chabard. Projet N3S - manuel de la version 3, 1991. Tech. Rep. EDF HE-41/91.30B, Electricité de France.

[15] L. Ignat, D. Pelletier, and F. Ilinca. Adaptive computation of turbulent forced convection. *Numerical Heat Transfer, Part A*, 34:847–871, 1998.

[16] J.A. Schetz. *Boundary Layer Analysis*. Prentice Hall, 1993.

[17] R. Duvigneau and D. Pelletier. On the accuracy of shape parameter boundary conditions in the sensitivity equation method. In *43rd AIAA Aerospace Sciences Meeting and Exhibit*, Reno, NV, January 2004. AIAA Paper 2005-0127.

[18] A. N. Brooks and T. J. R. Hughes. Streamline upwind/petrov-galerkin formulations for convection dominated flows with particular emphasis on the incompressible navier-stokes equations. *Computer Methods in Applied Mechanics and Engineering*, 32:199–259, 1982.

[19] F. Ilinca, J.-F. Hétu, and D. Pelletier. On stabilized finite element formulations for incompressible advective-diffusive transport and fluid flow problems. *Computer Methods in Applied Mechanics and Engineering*, 188(1):235–257, 2000.

[20] J. Peraire, M. Vahdati, K. Morgan, and O.C. Ziekiewicz. Adaptive remeshing for compressible flow computations. *Journal of Computational Physics*, 72(2):449–466, 1987.

[21] D. Pelletier. Adaptive finite element computations of complex flows. *International Journal for Numerical Methods in Fluids*, 31:189–202, 1999.

[22] J. Z. Zhu and O. C. Zienkiewicz. A simple error estimator and adaptive procedure for pratical engineering analysis. *International Journal for Numerical Methods Engineering*, 24:337–357, 1987.

[23] J. Z. Zhu and O. C. Zienkiewicz. The Superconvergente Patch Recovery and a posteriori error estimates. *International Journal for Numerical Methods Engineering*, 33:1331–1364, 1992.

[24] M. Ainsworth and J. T. Oden. *A posteriori error estimation in Finite Element analysis*. Wiley & Sons, New York, 2000.

[25] R. Verfürth. *A review of a posteriori error estimation and adaptive mesh refinement techniques*. Wiley-Teubner, New York-Stuttgart, 1996.

[26] A. Hay and D. Pelletier. Code and solution verification of an adaptive finite element turbulent flow solver. In *18th AIAA Computational Fluid Dynamics Conference*, Miami, FL, June 2007. AIAA-2007-4202.

[27] É. Turgeon, D. Pelletier, and J. Borggaard. A continuous sensitivity equation approach to optimal design in mixed convection. In *33rd AIAA Thermophysics Conference*, Norfolk, VA, Jun.-Jul. 1999. AIAA Paper 99-3625.

[28] L. Eça, M. Hoekstra, A. Hay, and D. Pelletier. A manufactured solution for a two-dimensional steady wall-bounded incompressible turbulent flow. In *7th World Congress on Computational Mechanics, Accomplishments and Challenges in Verification & Validation*, Los Angeles, July 2006.

[29] L. Eça, M. Hoekstra, A. Hay, and D. Pelletier. On the construction of manufactured solutions for one and two-equation eddy-viscosity models. *International Journal for Numerical Methods in Fluids*, 54(2):119–154, 2007.

[30] L. Eça, M. Hoekstra, A. Hay, and D. Pelletier. Verification of RANS solvers with manufactured solutions, 2007. Engineering with computers, Published on-line.

[31] R. Duvigneau and D. Pelletier. On accurate boundary conditions for a shape sensitivity equation method. *International Journal for Numerical Methods in Fluids*, 56(2):147–164, 2006.

[32] A. Hay and D. Pelletier. Second workshop on cfd uncertainty analysis : Results from the cadyf code. In *2nd Workshop on CFD Uncertainty Analysis*, Lisboa, Portugal, 0ctober 2006.

[33] L. Eça and M. Hoekstra. Results, discussion and conclusions of the 2nd Workshop on Uncertainty Analysis. In *2nd Workshop on Uncertainty Analysis*, Lisbon, Portugal, october 2006.

[34] É. Turgeon, D. Pelletier, S. Etienne, and J. Borggaard. Sensitivity and uncertainty analysis for turbulent flows. In *44th AIAA Aerospace Sciences Meeting and Exhibit*, Reno, NV, January 2002. AIAA Paper 2002-0985.

[35] D. Lacasse, É. Turgeon, and D. Pelletier. On the judicious use of the $k - \epsilon$ model, wall functions and adaptivity. In *39th AIAA Aerospace Sciences Meeting and Exhibit*, Reno, NV, Jan. 2001. AIAA Paper 2001-0882.

Paper No. 8

Discusser's Name: Chris Roy

Question:
1) How can the observed order of accuracy be computed for the flat plate case without uniform mesh refinement?
2) For the square cylinder case, were the solutions steady-state or unsteady? Note, that there is a strong non-turbulent instability when the cylinder is moved away from the wall.

Authors' Reply:

1) The strategy behind mesh adaptivity is to equidistribute the error over the computational domain. Complete error equidistribution is only possible when considering a single variable and can only be partial in a multi-variable context. Due to the equidistribution principle, strong local refinement is performed during the first adaptive cycles. However, after these cycles, the equidistribition can no longer be improved. Thus, the last adaptive steps almost correspond to uniform refinement for reducing the global error and allow for the calculation of the observed orders of accuracy. Note that, for another study, we have used a set of uniformly refined grids. The conclusion of the code verification was quite similar including the computed observed orders of accuracy.

2) We have only addressed gap heights for which flows are reported steady by experimental studies. Indeed, the baseline gap size is S/D=0.25 and we have considered perturbations in this parameter up to 10%. Hence all cases are far from the onset of the instability that is reported around S/D=0.4.

Discusser's Name: William Oberkampf

Question: What error estimator was used that only gave an order of magnitude estimate of the solution error?

Authors' Reply:

We consider two different error estimators which are both single-grid recovery-based techniques:
i) The ZZ error estimator which provides elemental error norms for all variables (the semi-norm for the Taylor-Hood element)
ii) a Wibert type of error estimator which provide pointwise error estimations (that are more difficult to obtain than elemental error norms)
ZZ was used for diving the mesh adaptation procedure while "Wibert" was used to estimate the error on post-processed quantities (drag, pressure coefficient, recirculation length, local point variables, …)

On a manufactured solution that mimics a turbulent boundary layer, we report (with sufficient grid resolution):

- the ZZ estimator can reproduce the true error fairly well. Efficiency indexes are typically around 0.8 (and close to 1 for laminar problem)
- the Wibert error estimator computes the order of magnitude of the true error but does not provide one significant digit.